

Multidimensional Contrast Limited Adaptive Histogram Equalization

Vincent Stimper^{1,2,*}, Stefan Bauer¹, Ralph Ernstorfer³,
Bernhard Schölkopf¹ and R. Patrick Xian^{3,*}

¹Max Planck Institute for Intelligent Systems, 72072 Tübingen, Germany

²Physics Department, Technical University Munich, 85748 Garching, Germany

³Fritz Haber Institute of the Max Planck Society, 14195 Berlin, Germany

{vincent.stimper,stefan.bauer,bs}@tue.mpg.de, {ernstorfer,xian}@fhi-berlin.mpg.de

Abstract

Contrast enhancement is an important preprocessing technique for improving the performance of downstream tasks in image processing and computer vision. Among the existing approaches based on nonlinear histogram transformations, contrast limited adaptive histogram equalization (CLAHE) is a popular choice when dealing with 2D images obtained in natural and scientific settings. The recent hardware upgrade in data acquisition systems results in significant increase in data complexity, including their sizes and dimensions. Measurements of densely sampled data higher than three dimensions, usually composed of 3D data as a function of external parameters, are becoming commonplace in various applications in the natural sciences and engineering. The initial understanding of these complex multidimensional datasets often requires human intervention through visual examination, which may be hampered by the varying levels of contrast permeating through the dimensions. We show both qualitatively and quantitatively that using our multidimensional extension of CLAHE (MCLAHE) acting simultaneously on all dimensions of the datasets allows better visualization and discernment of multidimensional image features, as are demonstrated using cases from 4D photoemission spectroscopy and fluorescence microscopy. Our implementation of multidimensional CLAHE in Tensorflow is publicly accessible and supports parallelization with multiple CPUs and various other hardware accelerators, including GPUs.

I. Introduction

Contrast is instrumental for visual processing and understanding of the information content within images in various settings [1]. Therefore, computational methods for contrast enhancement (CE) are frequently used to improve the visibility of images [2]. Among the existing CE methods, histogram transform-based algorithms are popular due to their computational efficiency. A widely

adopted example in this class of CE algorithms is the contrast limited adaptive histogram equalization (CLAHE) [3; 4], originally formulated in 2D, which performs local adjustments of image contrast with low noise amplification. The contrast adjustments are interpolated between the neighboring rectilinear image patches called kernels and the spatial adaptivity in CLAHE is achieved through the selection of the kernel size. The intensity range of the kernel histogram set by a clip limit restrains the noise amplification in the outcome. The use cases of CLAHE and its variants range from underwater exploration [5], breast cancer detection in X-ray mammography [6; 7], video forensics [8] to charging artifact reduction in electron microscopy [9] and multichannel fluorescence microscopy [10]. Due to the original formulation, its applications are concentrated almost exclusively in fields and instruments producing 2D imagery.

However, the current data acquisition systems are capable of producing densely sampled image data at three or higher dimensions at high rates [11; 12; 13; 14], following the rapid progress in spectroscopic and imaging methods in the characterization of materials and biological systems. Sifting through the image piles to identify relevant features for scientific and engineering applications is becoming an increasingly challenging task. Despite the variety of experimental techniques, the parametric changes (with respect to time, temperature, pressure, wavelength, concentration, etc.) in the measured system resulting from internal dynamics or external perturbations are often translated into intensity changes registered by the imaging detector circuit [15]. Visualizing and accessing the multidimensional image features (static or dynamic) often begins with human visual examination, which are influenced by the contrast determined by the detection mechanism, specimen condition and instrument resolution. To assist multidimensional image processing and understanding, the existing CE algorithms formulated in 2D should adapt to the demands of higher dimensions (3D and above). Recently, a 3D extension of CLAHE has been described and shown to compare favorably over separate 2D CLAHE for volumetric (3D) imaging data both in visual inspection and in a contrast metric, the peak signal-to-noise ratio (PSNR) [16].

In this work, we formulate and implement multidimen-

*Contact Authors

sional CLAHE (MCLAHE), a flexible and efficient framework that generalizes the CLAHE algorithm to an arbitrary number of dimensions. The MCLAHE algorithm builds on the principles of CLAHE and, in addition, allows the use of arbitrary-shape rectilinear kernels and expands the spatial adaptivity of CLAHE to the intensity domain with adaptive histogram range selection, neither of which is present in the original formulation of 2D [3; 4] or 3D CLAHE [16]. Next, we demonstrate the effectiveness of MCLAHE using visual comparison and computational contrast metrics of two 4D (3D+time) datasets in materials science by photoemission spectroscopy [17] and in biological science by fluorescence microscopy [18], respectively. These two techniques are representatives of the current capabilities and complexities of multidimensional data acquisition methods in natural sciences. The use and adoption of CE in their respective communities will potentially benefit visualization and downstream data analysis. Specifically, in the photoemission spectroscopy dataset of electronic dynamics in a semiconductor material, we show that MCLAHE can drastically reduce the intensity anisotropy and enable visual inspection of dynamical features across the bandgap; In the fluorescence microscopy dataset of a developing embryo [19], we show that MCLAHE improves the visual discernibility of cellular dynamics from sparse labeling. In addition, we provide a Tensorflow [20] implementation of MCLAHE publicly accessible on GitHub [21], which enables the reuse and facilitates the adoption of the algorithm in a wider community.

The outline of the paper is as follows. In Section II, we summarize the developments in histogram equalization leading up to CLAHE and the use of contrast metrics in outcome evaluation. In Section III, we highlight the details of the MCLAHE algorithm that differentiate from previous lower-dimensional CLAHE algorithms. In Section IV, we describe the use cases of MCLAHE in photoemission spectroscopy and fluorescence microscopy. In Section V, we comment on the current limitations and potential improvements in the software implementation. Finally, in Section VI, we draw the conclusions.

II. Background and related work

Histogram transform-based CE began with the histogram equalization (HE) algorithm developed by Hall in 1974 [22], where a pixelwise intensity mapping derived from the normalized cumulative distribution function (CDF) of the entire image’s intensity histogram is used to reshape the histogram into a more uniform distribution [22; 23]. However, Hall’s approach derives the intensity histogram globally, which can overlook fine-scale image features of varying contrast. Subsequent modifications to HE introduced independently by Ketcham [24] and Hummel [25], named the adaptive histogram equalization (AHE) [3], addressed this issue by using the intensity histogram of a rectangular window, called the *kernel*, or the contextual region, around each pixel to estimate the intensity mapping. However, AHE comes with significant computational

overheads due to the many kernel histograms involved. In performance, the noise in regions with relatively uniform intensities tends to be overamplified. Pizer *et al.* proposed a version of AHE [3] with much less computational cost by using only the adjoining kernels that divide up the image for local histogram computation and intensity mapping determination, followed by nearest-neighbor interpolation to other pixels not centered on a kernel. Moreover, they introduced the histogram clip limit to constrain the intensity redistribution and suppress noise amplification [3; 4]. The 3D extension of CLAHE was recently introduced by Amorim *et al.* [16] for medical imaging applications. Their algorithm uses volumetric kernels to compute the local histograms and trilinear interpolation to derive the voxelwise intensity mappings from nearest-neighbor kernels. Qualitative results were demonstrated on magnetic resonance imaging data, showing that the volumetric CLAHE leads to a better contrast than applying 2D CLAHE separately to every slice of the data. Unfortunately, their code is not in the public domain for further use and testing.

Evaluating the outcome of contrast enhancement requires quantitative metrics of image contrast, which are rarely used in the early demonstrations of HE algorithms [3; 22; 24; 25; 26; 27] because the use cases are predominantly in 2D and the improvements of image quality are largely intuitive. In domain-specific settings involving higher-dimensional (3D and above) imagery, intuition becomes less suitable for making judgments, but computational contrast metrics can provide guidance for evaluation. The commonly known contrast metrics include the mean squared error (MSE) (or the related PSNR) [28; 29], the standard deviation (or the root-mean-square contrast) [30] and the Shannon entropy (or the grey-level entropy) [31]. These metrics are naturally generalizable to imagery in arbitrary dimensions [32] and are easy to compute. We also note that despite the recently developed 2D image quality assessment scores based on the current understanding of human visual systems [28; 31] proved to be more effective than the classic metrics we choose to quantify contrast, their generalization and relevance to the evaluation of higher-dimensional images obtained in natural sciences and engineering settings, often without undistorted references, are not yet explored, so they are not used here for comparison of results.

III. Methods

A. Overview

Extending CLAHE to multiple dimensions requires to address some of the existing limitations of the 2D (or 3D) version of the algorithm. (1) The formulation of 2D [3; 4] and 3D CLAHE [16] involve explicit enumerated treatment of image boundaries, which becomes tedious and unscalable in arbitrary dimensions because the number of distinct boundaries scales exponentially as $3^D - 1$ with respect to the number of dimensions D . We resolve this issue by introducing data padding in MCLAHE as an initial step

such that every D -dimensional pixel lives in an environment with equal size in the augmented data (see Section III.B). The data padding also enables the choice of kernels with an arbitrary size smaller than the original data. (2) The formalism for calculating and interpolating the intensity mapping needs to be generalized to arbitrary dimensions. We present a unified formulation using the Lagrange form of multilinear interpolation [33] that includes the respective use of bilinear and trilinear interpolation in 2D [3; 4] and 3D [16] versions of CLAHE as special cases in lower dimensions (see Section III.C). (3) To further suppress noise amplification in processing image data containing vastly different intensity features, we introduce adaptive histogram range (AHR), which extends the spatial adaptivity of the original CLAHE algorithm to the intensity domain. AHR allows the choice of local histogram range according to the intensity range of each kernel instead of using a global histogram range (GHR) (see Section III.D).

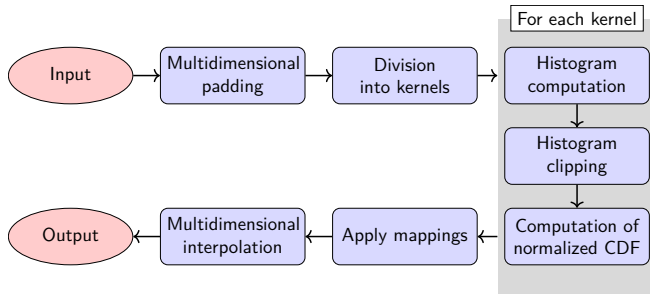


Figure 1: Schematic of the MCLAHE algorithm.

The MCLAHE algorithm is summarized graphically in Fig. 1 and in pseudocode in Algorithm 1. It operates on input data of dimension D , where D is a positive integer. Let s_i be the size of data along the i th dimension, so $i \in \{0, \dots, D-1\}$. The algorithm begins with padding of the input data around the D -dimensional edges. The padded data is then kernelized, or divided into adjoining rectilinear kernels with dimension D and a size of b_i along the i th dimension defined by the user. In each kernel, we then separately compute and clip its intensity histogram and obtain the normalized CDF. The intensity mapping at each D -dimensional pixel is computed by multilinear interpolation of the transformed intensities among the normalized CDFs in its nearest-neighbor kernels. Finally, the contrast-enhanced output data is generated by carrying out the same procedure for all pixels in the input data.

B. Multidimensional padding

Due to the exponential scaling of the distinct boundaries as $3^D - 1$ with the data dimension D , we use multidimensional padding to circumvent the enumerated treatment of boundaries and ensure that the data can be divided into integer multiples of the user-defined kernel size. The padding is composed of two parts. We discuss the case for D dimensions and illustrate with an example for $D = 2$ in Fig. 2(c). Firstly, we require that the intensity histogram

Algorithm 1 Formulation of the MCLAHE procedure in pseudocode. Here, $//$ denotes the integer division operator, cdf the cumulative distribution function, and map the intensity mappings applied to the high dimensional pixels.

Input: data_in

Parameters: kernel_size (array of integers for all kernel dimensions), clip_limit (threshold value in $[0, 1]$ for clipping the local histograms), n_bins (number of bins of the local histograms)

Output: data_out

```

1:  $\text{pad\_len} = 2 \cdot \text{kernel\_size} - 1 + ((\text{shape}(\text{data\_in}) - 1) \bmod \text{kernel\_size})$ 
2:  $\text{data\_hist} = \text{pad\_symmetric}(\text{data\_in}, [\text{pad\_len} // 2, (\text{pad\_len} + 1) // 2])$ 
3:  $\text{b\_list} = \text{split } \text{data\_hist} \text{ into kernels of size } \text{kernel\_size}$ 
4: for each  $\text{b}$  in  $\text{b\_list}$  do
5:    $\text{h} = \text{histogram}(\text{b}, \text{n\_bins})$ 
6:   Redistribute weight in  $\text{h}$  above  $\text{clip\_limit}$  equally across  $\text{h}$ 
7:    $\text{cdf\_b} = \text{cdf}(\text{h})$ 
8:    $\text{map}[\text{b}] = (\text{cdf\_b} - \min(\text{cdf\_b})) / (\max(\text{cdf\_b}) - \min(\text{cdf\_b}))$ 
9: end for
10: for each neighboring kernel do
11:   for each pixel  $\text{p}$  in  $\text{data\_in}$  do
12:      $\text{u} = \text{map}[\text{b in neighboring kernel of p}](\text{p})$ 
13:     for  $\text{d} = 0 \dots D-1$  do
14:        $\text{u} = \text{u} \cdot (\text{coefficient of the neighboring kernel in dimension } \text{d})$ 
15:     end for
16:     Assign  $\text{u}$  to pixel  $\text{p}$  in  $\text{data\_out}$ 
17:   end for
18: end for
19: return  $\text{data\_out}$ 

```

of each kernel is computed with the same number of D -dimensional pixels. Therefore, the size of the padded data should be an integer multiple of the kernel size. For each dimension, if s_i is not an integer multiple of b_i , a padding of $b_i - (s_i \bmod b_i)$ is needed. To absorb the case when $s_i \bmod b_i \equiv 0$, we add a shift of -1 to the expression. Therefore, the padding required along the i th dimension of the kernel to make the data size divisible by the kernel size is $b_i - 1 - ((s_i - 1) \bmod b_i)$. Secondly, we require that every D -dimensional pixel in the original data have the same number of nearest-neighbor kernels such that the pixels at the border do not need a special treatment in the interpolation step. Therefore, we need to pad, in addition, by the kernel size, b_i , along the i th dimension. To satisfy both requirements, the total padding length along the i th dimension, p_i , is

$$p_i = 2b_i - 1 - ((s_i - 1) \bmod b_i). \quad (1)$$

This length is split into two parts, p_{i0} and p_{i1} , and attached to the start and end of each dimension, respectively.

$$\begin{aligned} p_{i0} &= p_i / 2, \\ p_{i1} &= (p_i + 1) / 2. \end{aligned} \quad (2)$$

Here, the $//$ sign denotes integer division. To keep the local intensity distribution at the border of the image unchanged, the paddings are added symmetrically along the boundaries of the data. The padding procedure is described in lines 1–2 in Algorithm 1.

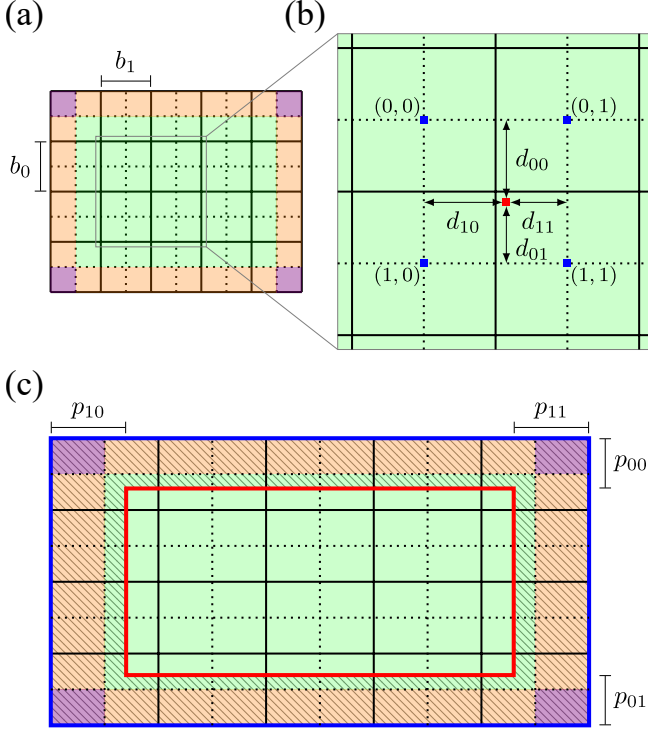


Figure 2: Illustration of the concepts related to the MCLAHE algorithm in 2D. In (a)-(c) the image is equipartitioned into kernels of size (b_0, b_1) bounded by solid black lines. The dotted black lines indicate regions with pixels having the same nearest-neighbor kernels. Color coding is used to specify the types of border regions, with the areas in green, orange and magenta having four, two and one nearest-neighbor kernels, respectively. A zoomed-in region of (a) is shown in (b). The red square mark in (b) represents a pixel under consideration and the four blue square marks represent the closest kernel centers next to the red one. The padded image is shown in (c) with the original image now bounded by solid red lines and the padding is indicated by the hatchings. The padding lengths in 2D are labeled as p_{00} , p_{01} , p_{10} , p_{11} in (c) and their values are calculated using Eq. (2).

C. Multidimensional interpolation

To derive a generic expression for the intensity mapping in arbitrary dimensions, we start with the example in 2D CLAHE, where each pixel intensity I_n (n being the pixel or voxel index) is transformed by a bilinear interpolation of the mapped intensities obtained from the normalized CDF of the nearest-neighbor kernels [3; 4]. We introduce the kernel index $\mathbf{i} = (i_0, i_1) \in \{0, 1\}^2$. The values of 0 and 1 in the binary alphabet $\{0, 1\}$ represent the two sides (i.e. above and below) in a dimension divided by the pixel in consideration. For the 2D case, (i_0, i_1) takes the values of

$(0, 0)$, $(0, 1)$, $(1, 0)$ and $(1, 1)$, as shown in Fig. 2(b). Let $m_{\mathbf{i}}$ be the intensity mapping obtained from the kernel with the index \mathbf{i} .

$$m_{\mathbf{i}}(I_n) = \widehat{\text{CDF}}_{\mathbf{i}}(I_n), \quad (3)$$

where $\widehat{\text{CDF}}_{\mathbf{i}}$ represents the normalized CDF obtained from the clipped histogram of the kernel with the index \mathbf{i} . As shown in Fig. 2(b), the bilinear interpolation at the pixel in consideration located at the red square mark are computed using the four nearest-neighbor kernels centered on the blue square mark. The interpolation coefficients, $c_{\mathbf{i}}$, can be represented as Lagrange polynomials [34; 33] using the kernel size (b_0, b_1) and the distances $(d_{00}, d_{01}, d_{10}, d_{11})$ between the pixel and the kernel centers in the two dimensions.

$$c_{00} = \frac{(b_0 - d_{00})(b_1 - d_{10})}{b_0 b_1}, \quad (4)$$

$$c_{01} = \frac{(b_0 - d_{00})(b_1 - d_{11})}{b_0 b_1}, \quad (5)$$

$$c_{10} = \frac{(b_0 - d_{01})(b_1 - d_{10})}{b_0 b_1}, \quad (6)$$

$$c_{11} = \frac{(b_0 - d_{01})(b_1 - d_{11})}{b_0 b_1}. \quad (7)$$

The transformed intensity \tilde{I}_n from I_n is given by

$$\tilde{I}_n = c_{00}m_{00}(I_n) + c_{01}m_{01}(I_n) + c_{10}m_{10}(I_n) + c_{11}m_{11}(I_n). \quad (8)$$

Equation (4)-(7) and (8) can be rewritten in a compact form using the kernel index \mathbf{i} introduced earlier,

$$\tilde{I}_n = \sum_{\mathbf{i} \in \{0, 1\}^2} c_{\mathbf{i}} m_{\mathbf{i}}(I_n), \quad (9)$$

$$c_{\mathbf{i}} = \prod_{j=0}^1 \frac{b_j - d_{ji_j}}{b_j}. \quad (10)$$

In the 2D case, the term d_{ji_j} takes on the value d_{ji_0} or d_{ji_1} . The choice of i_0 and i_1 from the binary alphabet $\{0, 1\}$ in d_{ji_j} follows that of the index \mathbf{i} . The special cases of transforming the border pixels in the image are naturally resolved in our case after data padding (see Section III.B).

In D dimensions, the kernel index $\mathbf{i} = (i_0, i_1, \dots, i_{D-1}) \in \{0, 1\}^D$. Analogous to the two-dimensional case described before, the intensity mapping of each D -dimensional pixel is now calculated by multilinear interpolation between the 2^D nearest-neighbor kernels in all dimensions.

$$\tilde{I}_n = c_{00\dots 0}m_{00\dots 0}(I_n) + c_{00\dots 1}m_{00\dots 1}(I_n) + c_{11\dots 0}m_{11\dots 0}(I_n) + c_{11\dots 1}m_{11\dots 1}(I_n). \quad (11)$$

Similarly, (11) and the corresponding expressions for the interpolation coefficients can be written in the compact form as

$$\tilde{I}_n = \sum_{\mathbf{i} \in \{0, 1\}^D} c_{\mathbf{i}} m_{\mathbf{i}}(I_n), \quad (12)$$

$$c_{\mathbf{i}} = \prod_{j=0}^{D-1} \frac{b_j - d_{ji_j}}{b_j}. \quad (13)$$

The formalism is very similar to that of the 2D case (see (8)-(10)), yet allows us to generalize to arbitrary dimension with only an update to the kernel index i . In Algorithm 1, the calculation of intensity mappings through interpolation is described in lines 12–15.

D. Adaptive histogram range

In the original formulation of CLAHE in 2D [3; 4], the local histogram ranges for all kernels are the same, which works well when the kernels contain intensities in a similarly wide range. Tuning of the trade-off between noise amplification and the signal enhancement is then achieved through the kernel size and the clip limit [29]. However, if different patches of the image data contain local features within distinct narrow intensity ranges, they may accumulate in very few histogram bins set globally, which then will require a high clip limit to enhance and therefore comes with the price of noise amplification in many parts of the data. This problem may be ameliorated by adaptively choosing the local histogram range to lie within the minimum and maximum of the intensity values of the kernel, while keeping the number of bins the same for all kernels. An example use case of the AHR is presented in Section IV.A.

IV. Applications

We now apply the MCLAHE algorithm to two cases in the natural sciences that involve large densely sampled 4D (3D+time) data. Each example includes a brief introduction of the background knowledge on the type of measurement, the resulting image data features and the motivation for the use of contrast enhancement, followed by discussion and comparison of the outcome using MCLAHE. The performance details are provided at the end of each example.

A. Photoemission spectroscopy

Background information. In photoemission spectroscopy, the detector registers electrons liberated by intense vacuum UV or X-ray pulses from a solid state material sample [17]. The measurement is carried out in the so-called 3D momentum space, spanned by the coordinates (k_x, k_y, E) , in which k_x, k_y are the electron momenta and E the energy. The detected electrons form patterns carrying information about the anisotropic electronic density distribution within the material. The fourth dimension in time-resolved photoemission spectroscopy represent the waiting time in observation since the electronic system is subject to an external perturbation (i.e. light excitation). In the image data acquired in photoemission spectroscopy, the inhomogeneous intensity modulation from the experimental geometry, light-matter interaction [35] and scattering background creates contrast variations within and between the so-called energy bands, which manifest themselves as intercrossing band-like curves (in 2D) or surfaces (in 3D) blurred by convolution with the instrument response function and further affected by other factors such as the sample quality and the dimensionality of the electronic system, etc [17]. Visualization and

demarcation of the band-like image features are of great importance for understanding the momentum-space electronic distribution and dynamics in multidimensional photoemission spectroscopy [14]. However, in addition to the physical limitations on the contrast inhomogeneities listed before, the intensity difference between the lower bands (or valence bands) and the upper bands (or conduction bands) on the energy scale is on the order of 100 or higher and varies by the materials under study and light excitation conditions. To improve the image contrast in multiple dimensions, we applied MCLAHE to a 4D (3D+time) dataset measured for the time- and momentum-resolved electron dynamics of tungsten diselenide (WSe_2), a semiconductor material with highly dispersing electronic bands [36]. The 4D data are obtained from an existing experimental setup [37] and processed using a custom pipeline [38; 39] from registered single photoelectron events. For comparison of contrast enhancement, we apply both 3D and 4D CLAHE to the 4D photoemission spectroscopy data. In the case of 3D CLAHE, the algorithm is applied to the 3D data at each time frame separately. The raw data and the results are shown in Fig. 3, along with the contrast metrics computed and listed in Table 1.

Results and discussion. The original photoemission spectroscopy data are visualized poorly on an energy scale covering both the valence and conduction bands, as shown in Fig. 3(a)-(d). The situation is much improved in the MCLAHE-processed data shown in Fig. 3(e)-(l), where the population dynamics in the conduction band of WSe_2 [40; 41] and the band broadening in the valence bands are sufficiently visible to be placed on the same colorscale, allowing to identify and correlate fine features of the momentum-space dynamics. The improvement is also reflected quantitatively in Table 1 in the drastic increase in MSE and, correspondingly, the drop in the PSNR and standard deviation between the unadjusted (smoothed) and contrast-enhanced data. Furthermore, visual comparison of the results in Fig. 3(e)-(l) show that noise enhancement is less severe when applying 4D CLAHE though unavoidable to some extent due to the weakness of the dynamical signal. This is represented in the slight decrease in MSE or, equivalently, the slight increase in PSNR between the 3D and 4D CLAHE-processed data. Finally, the processing also compares the use of AHR and GHR in dataset including drastically different intensity features, which in this case are represented by the valence and conduction bands. The inclusion of AHR compares favorably over GHR (not shown in Fig. 3) in both the 3D and 4D scenarios as indicated in the improvement in all contrast metrics in Table 1. The improvement comes from correctly accounting for the large intensity variations in different regions of the image.

To quantify the influence of contrast enhancement on the dynamical features in the data, we calculated the integrated intensity in the conduction band of the data in all three cases and the results are summarized in Fig. 3(m)-(o). The standard score in Fig. 3(o) is used to compare the integrated signals in a scale-independent fashion. The dynamics represented in the intensity changes are better

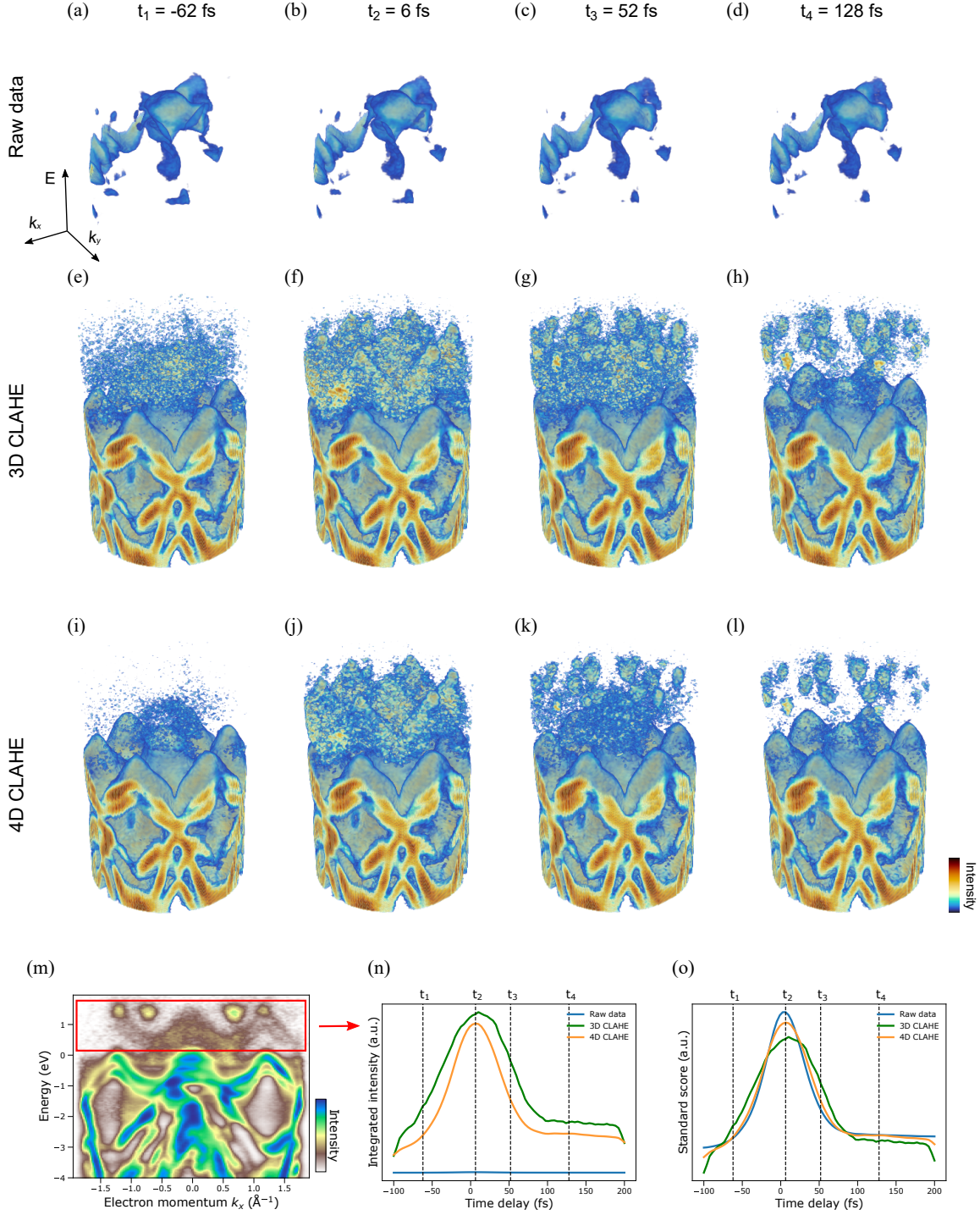


Figure 3: Applications of MCLAHE to 4D (3D+time) photoemission spectroscopy data including the temporal evolution of the electronic band structure of the semiconductor WSe_2 during and after optical excitation (see Section IV.A). Four time steps in the 4D time series are selected for visualization including the raw data in (a)-(d), the 3D CLAHE-processed data in (e)-(h) and the 4D CLAHE-processed data in (i)-(l). The adaptive histogram range (AHR) setting in the MCLAHE algorithm were included in the data processing. All 3D-rendered images in (a)-(l) share the same color scaling shown in (l). The integrated dynamics in (n)-(o) over the region specified by the box in (m) over the 3D momentum space show that the 4D CLAHE amplifies less noise while better preserves the dynamical timescale than the 3D CLAHE, in comparison with the original data.

preserved in 4D than 3D CLAHE-treated data and the former are less influenced by the boundary artifacts in the beginning and at the end of the time delay range. These observations reinforce the argument that 4D CLAHE is superior to its 3D counterpart overall in content-preserving contrast enhancement.

Table 1: Contrast metrics for photoemission spectroscopy data

Dataset	MSE	PSNR	STD	ENT
Raw	-	-	0.0667	2.294
Smoothed	0.0015	166.63	0.0938	2.615
3D CLAHE (GHR)	0.0426	152.18	0.2296	3.048
4D CLAHE (GHR)	0.0428	152.16	0.2299	3.049
3D CLAHE (AHR)	0.1121	147.98	0.2838	4.471
4D CLAHE (AHR)	0.1050	148.26	0.2818	4.387

MSE: mean square error. PSNR: peak signal-to-noise ratio. STD: standard deviation. ENT: Shannon entropy.

Processing details. The raw 4D photoemission spectroscopy data have a size of $180 \times 180 \times 300 \times 80$ in the (k_x, k_y, E, t) dimensions. They are first denoised using a Gaussian filter with standard deviations of 0.7, 0.9 and 1.3 along the momenta, energy and time dimensions, respectively. For both the application of 3D and 4D CLAHE, we used a clip limit of 0.02 and local histograms with 256 grey-level bins. The kernel size for 4D CLAHE was (30, 30, 15, 20) and for 3D CLAHE the same kernel size for the first three dimensions, or (k_x, k_y, E) was used. Both GHR and AHR settings were used for comparison. The processing ran on a server with 64 Intel Xeon CPUs at 2.3 GHz and 254GB RAM. Running the 4D CLAHE procedure on the whole dataset took about 5.3 mins. In addition, we benchmarked the performance of 4D CLAHE on a GPU (NVIDIA GeForce GTX 1070, 8GB RAM) connected to the same server by processing the first 25 time frames of the dataset. The processing took 34 s versus 104 s when using the 64 CPUs only, which represents a 3.1-fold speed-up.

B. Fluorescence microscopy

Background information. In 4D fluorescence microscopy, the measurements are carried out in the Cartesian coordinates of the laboratory frame, or (x, y, z) , with the fourth dimension representing the observation time t . In practice, the photophysics of the fluorophores [42], the autofluorescence background [18] from the unlabeled part of the sample and the detection method, such as attenuation effect from scanning measurements at different depths or nonuniform illumination of fluorophores [43], pose a limit on the achievable image contrast in the experiment. The image features in fluorescence microscopy data often include sparsely labeled cells and cellular components such as the nuclei, organelles, membrane or dendrite structures. The limited contrast may render the downstream data annotation tasks, such as segmentation, tracking and lineage tracing [44; 45], challenging. Therefore, a digital contrast

enhancement method is potentially useful to improve the visibility of the cells and their corresponding dynamics. We demonstrate the use of MCLAHE for this purpose on a publicly available 4D (3D+time) fluorescence microscopy dataset [19] of embryo development of the ascidian (*Phallusia mammillata*), or sea squirt. The organism is stained and imaged *in toto* to reveal its development from a gastrula to tailbud formation with cellular resolution [19]. During embryo development, the fluorescence contrast exhibits time dependence due to cellular processes such as division and differentiation. We used the data from one fluorescence color channel containing the nuclei and processed through the MCLAHE pipeline. The results are compared with the original data on the same colorscale in Fig. 4 and the corresponding contrast metrics are shown in Table 2.

Results and discussion. The intensities in the raw fluorescence microscopy data are distributed highly unevenly in the colorscale, as shown in Fig. 4(a)-(d). The MCLAHE-processed 4D time series show significant improvement in the visibility of the cells against the background signal (e.g. autofluorescence, detector dark counts, etc). This is reflected in the surge in MSE, an increase in standard deviation and a drop in PSNR as shown in Table 2. In contrast to the previous example, in processing the embryo development dataset, the AHR option in MCLAHE was not used because the cellular feature sizes and their fluorescence intensities are similar throughout the organism, additionally, the dynamic range of the data is limited (see following discussion in Processing details) and the changes in fluorescence during development are relatively small. The initial high Shannon entropy of the raw data in Table 2 is due to its high background noise, which is reduced after smoothing, as indicated by the sharp drop in the entropy while the standard deviation show relative consistency. Then, the use of MCLAHE increases the entropy again, together with the large changes in other metrics, this time due to the contrast enhancement. Similarly to the previous example, the 4D CLAHE outperforms its 3D counterpart overall because of the lower MSE or, equivalently, the higher PSNR of the 4D results, indicating a higher similarity to the raw data. In other contrast metrics such as the standard deviation and the Shannon entropy, the 4D and 3D results have very close values, indicating the complexity of judging image contrast by a single metric. Visualization of the dynamics in Fig. 4(e)-(l) also shows that the 4D CLAHE-processed data preserve more of the fluorescence intensity change than its 3D counterpart, which still maintaining a high cell-to-background contrast. The contrast-enhanced embryo development data potentially allows better tracking of cellular lineage and dynamics [45; 46] that are challenging due to sparse fluorescent labeling.

Processing details. The raw 4D fluorescence microscopy data have a size of $512 \times 512 \times 109 \times 144$ in the (x, y, z, t) dimensions. They are first denoised by a median filter with the kernel size (2, 2, 2, 1). For 4D CLAHE, the kernel size of choice was (20, 20, 10, 25) and the same kernel size in the first three dimensions were used for 3D CLAHE

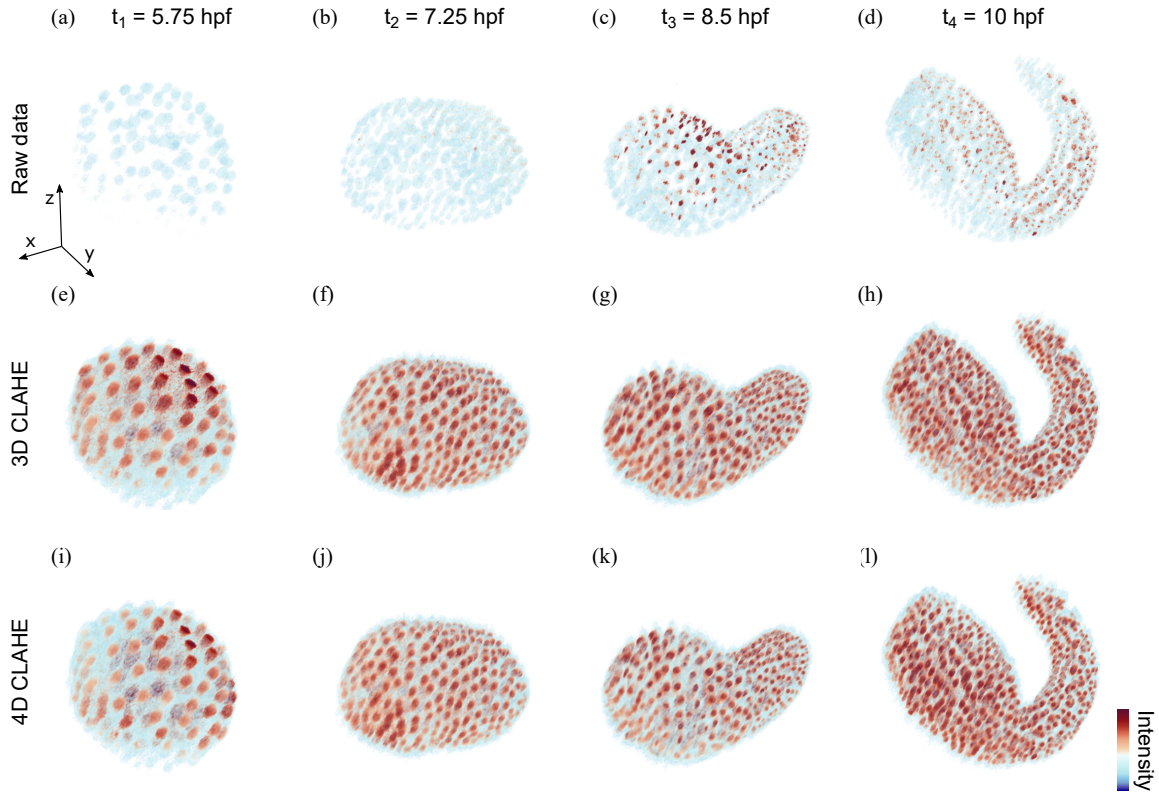


Figure 4: Applications of MCLAHE to 4D (3D+time) fluorescence microscopy data of the embryo development of ascidian (*Phallusia mammillata*), or sea squirt. Four time frames (hpf = hours post fertilization) in the 4D time series are visualized here for comparison, including the raw data in (a)-(d), the 3D CLAHE-processed data in (e)-(h) and the 4D CLAHE-processed data in (i)-(l). All images in (a)-(l) are rendered in 3D with the same color scaling shown in (l). Both MCLAHE-processed data show drastic improvement in the image contrast, while 4D CLAHE-processed data better preserves the dynamical intensity features from cellular processes.

Table 2: Contrast metrics for fluorescence microscopy data

Dataset	MSE($\times 10^{-3}$)	PSNR	STD	ENT
Raw	-	-	0.0316	1.1284
Smoothed	0.300	173.7	0.0265	0.5141
3D CLAHE	7.767	159.6	0.1048	0.5262
4D CLAHE	5.667	160.9	0.0921	0.5241

to allow a direct comparison. For both procedures, the clip limit was set at 0.25 and the number of histogram bins at 256. The intensities in the raw data were given as 8 bit unsigned integers resulting in only 256 possible values. Hence, only the GHR setting was used because the AHR setting would result in bins smaller than the resolution of the data. Processing using MCLAHE ran on the same server as for the photoemission spectroscopy data. The runtime using the 64 CPUs was about 26 mins. With the same setting as in the photoemission case study, processing of the first 8 time frames of the dataset took 32 s on the same GPU used previously versus 85 s on 64 CPUs, which represents a 2.7-fold speed-up.

V. Perspectives

While we have presented the applications of the MCLAHE algorithm to real-world datasets of up to multiple gigabytes in size, its current major performance limitation is in the memory usage, since the data needs to be loaded entirely into the RAM (of CPUs or GPUs), which may be challenging for very large imaging and spectroscopy datasets on the multi-terabyte scale that are becoming widely available [11]. Future improvements on the algorithm implementation may include distributed handling of chunked datasets to enable operation on hardware with the RAM to load only a subset of the data. In addition, the number of nearest-neighbor kernels currently required for intensity mapping interpolation increases exponentially with the number of data dimension D (see Section III.C). For datasets with $D < 10$, this may not pose a outstanding issue, but for even higher-dimensional datasets, new strategies may be developed for approximate interpolation of selected neighboring kernels to alleviate the exponential scaling.

Moreover, the applications of MCLAHE are not limited by the examples given in this work but are open to other types of data. It is especially beneficial to preprocessing of high dimensional data with dense sampling produced by various fast volumetric spectroscopic and imaging techniques [47; 48; 49; 50; 51] for improving the performance of feature annotation and extraction tasks.

VI. Conclusion

We present a flexible framework to extend the CLAHE algorithm to arbitrary dimensions for contrast enhancement of complex multidimensional imaging and spectroscopy datasets. We demonstrate the effectiveness of our algorithm, the multidimensional CLAHE, by visual analysis and

contrast quantification in case studies drawn from different measurement techniques with the capabilities of producing densely sampled high dimensional data, namely, 4D (3D+time) photoemission spectroscopy and 4D fluorescence microscopy. In the example applications, our algorithm greatly improves and balances the visibility of image features in diverse intensity ranges and neighborhood conditions. We further show that the best overall performance in each case comes from simultaneous application of multi-dimensional CLAHE to all data dimensions. In addition, we provide the implementation of multidimensional CLAHE in an open-source codebase to assist its reuse and integration into existing image analysis pipelines in various domains of natural sciences and engineering.

Acknowledgments

We thank the S. Schülke, G. Schnapka at the GNZ (Gemeinsames Netzwerkzentrum) in Berlin and M. Rapp at the MPCDF (Max Planck Computing and Data Facility) in Garching for computing supports. We thank S. Dong and S. Beaulieu for performing the photoemission spectroscopy measurement on tungsten diselenide at the Fritz Haber Institute. V. Stimper thanks U. Gerland for administrative support. The work has received funding from the Max Planck Society, including BiGmax, the Max Planck Society's Research Network on Big-Data-Driven Materials Science, and funding from the European Research Council (ERC) under the European Union's Horizon 2020 research and innovation program (Grant Agreement No. ERC-2015-CoG-682843).

References

- [1] B. Olshausen and D. Field, "Vision and the coding of natural images," *American Scientist*, vol. 88, no. 3, p. 238, 2000. [Online]. Available: <http://www.americanscientist.org/issues/feature/2000/3/vision-and-the-coding-of-natural-images>
- [2] W. K. Pratt, *Digital Image Processing*, 4th ed. Wiley-Interscience, 2007.
- [3] S. M. Pizer, E. P. Amburn, J. D. Austin, R. Cromartie, A. Geselowitz, T. Greer, B. ter Haar Romeny, J. B. Zimmerman, and K. Zuiderveld, "Adaptive histogram equalization and its variations," *Computer Vision, Graphics, and Image Processing*, vol. 39, no. 3, pp. 355–368, 1987. [Online]. Available: <http://www.sciencedirect.com/science/article/pii/S0734189X8780186X>
- [4] K. Zuiderveld, "Contrast limited adaptive histogram equalization," in *Graphics Gems*. Elsevier, 1994, pp. 474–485. [Online]. Available: <https://linkinghub.elsevier.com/retrieve/pii/B9780123361561500616>
- [5] M. S. Hitam, W. N. J. H. W. Yussof, E. A. Awalludin, and Z. Bachok, "Mixture contrast limited adaptive histogram equalization for underwater image enhancement," in *2013 International Conference*

- on *Computer Applications Technology (ICCAT)*. IEEE, jan 2013, pp. 1–5. [Online]. Available: <http://ieeexplore.ieee.org/document/6522017/>
- [6] W. Morrow, R. Paranjape, R. Rangayyan, and J. Desautels, "Region-based contrast enhancement of mammograms," *IEEE Transactions on Medical Imaging*, vol. 11, no. 3, pp. 392–406, 1992. [Online]. Available: <http://ieeexplore.ieee.org/document/158944/>
- [7] E. D. Pisano, S. Zong, B. M. Hemminger, M. DeLuca, R. E. Johnston, K. Muller, M. P. Braeuning, and S. M. Pizer, "Contrast limited adaptive histogram equalization image processing to improve the detection of simulated spiculations in dense mammograms," *Journal of Digital Imaging*, vol. 11, no. 4, p. 193, Nov 1998. [Online]. Available: <https://doi.org/10.1007/BF03178082>
- [8] J. Xiao, S. Li, and Q. Xu, "Video-Based Evidence Analysis and Extraction in Digital Forensic Investigation," *IEEE Access*, vol. 7, pp. 55 432–55 442, 2019. [Online]. Available: <https://ieeexplore.ieee.org/document/8700194/>
- [9] K. Sim, Y. Tan, M. Lai, C. Tso, and W. Lim, "Reducing scanning electron microscope charging by using exponential contrast stretching technique on post-processing images," *Journal of Microscopy*, vol. 238, no. 1, pp. 44–56, apr 2010. [Online]. Available: <http://doi.wiley.com/10.1111/j.1365-2818.2009.03328.x>
- [10] A. McCollum and W. Clocksin, "Multidimensional histogram equalization and modification," in *14th International Conference on Image Analysis and Processing (ICIAP 2007)*. IEEE, sep 2007, pp. 659–664. [Online]. Available: <http://ieeexplore.ieee.org/document/4362852/>
- [11] W. Ouyang and C. Zimmer, "The imaging tsunami: Computational opportunities and challenges," *Current Opinion in Systems Biology*, vol. 4, pp. 105–113, aug 2017. [Online]. Available: <https://linkinghub.elsevier.com/retrieve/pii/S2452310017300537>
- [12] P. Pantazis and W. Supatto, "Advances in whole-embryo imaging: a quantitative transition is underway," *Nature Reviews Molecular Cell Biology*, vol. 15, no. 5, pp. 327–339, may 2014. [Online]. Available: <http://www.nature.com/articles/nrm3786>
- [13] O. Ersen, I. Florea, C. Hirlimann, and C. Pham-Huu, "Exploring nanomaterials with 3D electron microscopy," *Materials Today*, vol. 18, no. 7, pp. 395–408, sep 2015. [Online]. Available: <https://linkinghub.elsevier.com/retrieve/pii/S1369702115001200>
- [14] G. Schönhense, K. Medjanik, and H.-J. Elmers, "Space-, time- and spin-resolved photoemission," *Journal of Electron Spectroscopy and Related Phenomena*, vol. 200, pp. 94–118, apr 2015. [Online]. Available: <http://linkinghub.elsevier.com/retrieve/pii/S0368204815001243>
- [15] J. H. Moore, C. C. Davis, M. A. Coplan, and S. C. Greer, *Building Scientific Apparatus*, 4th ed. Cambridge University Press, 2009.
- [16] P. Amorim, T. Moraes, J. Silva, and H. Pedrini, "3D Adaptive Histogram Equalization Method for Medical Volumes," in *Proceedings of the 13th International Joint Conference on Computer Vision, Imaging and Computer Graphics Theory and Applications*. SciTePress, 2018, pp. 363–370. [Online]. Available: <http://www.scitepress.org/DigitalLibrary/Link.aspx?doi=10.5220/0006615303630370>
- [17] S. Hüfner, *Photoelectron Spectroscopy : Principles and Applications*, 3rd ed. Springer, 2003.
- [18] U. Kubitscheck, Ed., *Fluorescence Microscopy: From Principles to Biological Applications*, 2nd ed. Weinheim, Germany: Wiley-VCH Verlag GmbH & Co. KGaA, may 2017. [Online]. Available: <http://doi.wiley.com/10.1002/9783527687732>
- [19] E. Faure, T. Savy, B. Rizzi, C. Melani, O. Stašová, D. Fabrèges, R. Špir, M. Hammons, R. Čunderlík, G. Recher, B. Lombardot, L. Duloquin, I. Colin, J. Kollár, S. Desnoullez, P. Affaticati, B. Maury, A. Boyreau, J.-Y. Nief, P. Calvat, P. Vernier, M. Frain, G. Lutfalla, Y. Kergosien, P. Suret, M. Remešíková, R. Doursat, A. Sarti, K. Mikula, N. Peyriéras, and P. Bourguine, "A workflow to process 3D+time microscopy images of developing organisms and reconstruct their cell lineage," *Nature Communications*, vol. 7, no. 1, p. 8674, apr 2016. [Online]. Available: <http://www.nature.com/articles/ncomms9674>
- [20] M. Abadi, A. Agarwal, P. Barham, E. Brevdo, Z. Chen, C. Citro, G. S. Corrado, A. Davis, J. Dean, M. Devin, S. Ghemawat, I. Goodfellow, A. Harp, G. Irving, M. Isard, Y. Jia, R. Jozefowicz, L. Kaiser, M. Kudlur, J. Levenberg, D. Mané, R. Monga, S. Moore, D. Murray, C. Olah, M. Schuster, J. Shlens, B. Steiner, I. Sutskever, K. Talwar, P. Tucker, V. Vanhoucke, V. Vasudevan, F. Viégas, O. Vinyals, P. Warden, M. Wattenberg, M. Wicke, Y. Yu, and X. Zheng, "TensorFlow: Large-scale machine learning on heterogeneous systems," 2015, software available from tensorflow.org. [Online]. Available: <http://tensorflow.org/>
- [21] V. Stimper and R. P. Xian, "Multidimensional contrast limited adaptive histogram equalization," <https://github.com/VincentStimper/mclahe>, 2019.
- [22] E. L. Hall, "Almost uniform distributions for computer image enhancement," *IEEE Transactions on Computers*, vol. C-23, no. 2, pp. 207–208, Feb 1974.
- [23] P. K. Sinha, *Image Acquisition and Preprocessing for Machine Vision Systems*. SPIE press, 2012.
- [24] D. J. Ketcham, "Real-time image enhancement techniques," in *Seminar on Image Processing*, vol. 0074, 1976, pp. 1–6. [Online]. Available: <https://doi.org/10.1117/12.954708>

- [25] R. Hummel, "Image enhancement by histogram transformation," *Computer Graphics and Image Processing*, vol. 6, no. 2, pp. 184 – 195, 1977. [Online]. Available: <http://www.sciencedirect.com/science/article/pii/S0146664X77800117>
- [26] R. Dale-Jones and T. Tjahjadi, "A study and modification of the local histogram equalization algorithm," *Pattern Recognition*, vol. 26, no. 9, pp. 1373–1381, sep 1993. [Online]. Available: <https://linkinghub.elsevier.com/retrieve/pii/003132039390143K>
- [27] J. Stark, "Adaptive image contrast enhancement using generalizations of histogram equalization," *IEEE Transactions on Image Processing*, vol. 9, no. 5, pp. 889–896, may 2000. [Online]. Available: <http://ieeexplore.ieee.org/document/841534/>
- [28] Z. Wang, A. Bovik, H. Sheikh, and E. Simoncelli, "Image quality assessment: From error visibility to structural similarity," *IEEE Transactions on Image Processing*, vol. 13, no. 4, pp. 600–612, apr 2004. [Online]. Available: <http://ieeexplore.ieee.org/document/1284395/>
- [29] G. F. C. Campos, S. M. Mastelini, G. J. Aguiar, R. G. Mantovani, L. F. de Melo, and S. Barbon, "Machine learning hyperparameter selection for contrast limited adaptive histogram Equalization," *EURASIP Journal on Image and Video Processing*, vol. 2019, no. 1, p. 59, dec 2019. [Online]. Available: <https://jivp-urasipjournals.springeropen.com/articles/10.1186/s13640-019-0445-4>
- [30] E. Peli, "Contrast in complex images," *Journal of the Optical Society of America A*, vol. 7, no. 10, p. 2032, oct 1990. [Online]. Available: <https://www.osapublishing.org/abstract.cfm?URI=josaa-7-10-2032>
- [31] K. Gu, G. Zhai, W. Lin, and M. Liu, "The analysis of image contrast: From quality assessment to automatic enhancement," *IEEE Transactions on Cybernetics*, vol. 46, no. 1, pp. 284–297, jan 2016. [Online]. Available: <http://ieeexplore.ieee.org/document/7056527/>
- [32] A. Kriete, "Image quality considerations in computerized 2-D and 3-D microscopy," in *Multidimensional Microscopy*. New York, NY: Springer New York, 1994, pp. 209–230. [Online]. Available: http://link.springer.com/10.1007/978-1-4613-8366-6_{-}12
- [33] G. M. Phillips, *Interpolation and Approximation by Polynomials*, ser. CMS Books in Mathematics. New York, NY: Springer New York, 2003. [Online]. Available: <http://link.springer.com/10.1007/b97417>
- [34] E. Kreyszig, H. Kreyszig, and E. J. Norminton, *Advanced Engineering Mathematics*, 10th ed. Wiley, 2011.
- [35] S. Moser, "An experimentalist's guide to the matrix element in angle resolved photoemission," *Journal of Electron Spectroscopy and Related Phenomena*, vol. 214, pp. 29–52, jan 2017. [Online]. Available: <https://linkinghub.elsevier.com/retrieve/pii/S0368204816301724>
- [36] J. M. Riley, F. Mazzola, M. Dendzik, M. Michiardi, T. Takayama, L. Bawden, C. Granerød, M. Leandersson, T. Balasubramanian, M. Hoesch, T. K. Kim, H. Takagi, W. Meevasana, P. Hofmann, M. S. Bahramy, J. W. Wells, and P. D. C. King, "Direct observation of spin-polarized bulk bands in an inversion-symmetric semiconductor," *Nature Physics*, vol. 10, no. 11, pp. 835–839, nov 2014. [Online]. Available: <http://www.nature.com/articles/nphys3105>
- [37] M. Puppín, Y. Deng, C. W. Nicholson, J. Feldl, N. B. M. Schröter, H. Vita, P. S. Kirchmann, C. Monney, L. Rettig, M. Wolf, and R. Ernstorfer, "Time- and angle-resolved photoemission spectroscopy of solids in the extreme ultraviolet at 500 kHz repetition rate," *Review of Scientific Instruments*, vol. 90, no. 2, p. 023104, feb 2019. [Online]. Available: <http://aip.scitation.org/doi/10.1063/1.5081938>
- [38] R. P. Xian, L. Rettig, and R. Ernstorfer, "Symmetry-guided nonrigid registration: The case for distortion correction in multidimensional photoemission spectroscopy," *Ultramicroscopy*, vol. 202, pp. 133–139, jul 2019. [Online]. Available: <https://linkinghub.elsevier.com/retrieve/pii/S0304399118303474>
- [39] R. P. Xian, Y. Acremann, S. Y. Agustsson, M. Dendzik, K. Bühlmann, D. Curcio, D. Kutnyakhov, F. Pressacco, M. Heber, S. Dong, J. Demsar, W. Wurth, P. Hofmann, M. Wolf, L. Rettig, and R. Ernstorfer, "A distributed workflow for volumetric band mapping data in multidimensional photoemission spectroscopy," *to be submitted*, 2019.
- [40] R. Bertoni, C. W. Nicholson, L. Waldecker, H. Hübener, C. Monney, U. De Giovannini, M. Puppín, M. Hoesch, E. Springate, R. T. Chapman, C. Cacho, M. Wolf, A. Rubio, and R. Ernstorfer, "Generation and evolution of spin-, valley-, and layer-polarized excited carriers in inversion-symmetric WSe₂," *Physical Review Letters*, vol. 117, no. 27, p. 277201, dec 2016. [Online]. Available: <https://link.aps.org/doi/10.1103/PhysRevLett.117.277201>
- [41] M. Puppín, "Time- and angle-resolved photoemission spectroscopy on bidimensional semiconductors with a 500 kHz extreme ultraviolet light source," Ph.D. dissertation, Free University of Berlin, sep 2017. [Online]. Available: <https://refubium.fu-berlin.de/handle/fub188/23006?show=full>
- [42] B. Valeur and M. N. Berberan-Santos, *Molecular Fluorescence: Principles and Applications*, 2nd ed. Wiley-VCH, 2013. [Online]. Available: <https://www.wiley.com/en-us/Molecular+Fluorescence%7D3A+Principles+and+Applications%7D2C+2nd+Edition-p-9783527328376>
- [43] J. C. Waters, "Accuracy and precision in quantitative fluorescence microscopy," *The Journal of Cell Biology*,

vol. 185, no. 7, pp. 1135–1148, jun 2009. [Online]. Available: <http://www.jcb.org/lookup/doi/10.1083/jcb.200903097>

- [44] T. A. Nketia, H. Sailem, G. Rohde, R. Machiraju, and J. Rittscher, "Analysis of live cell images: Methods, tools and opportunities," *Methods*, vol. 115, pp. 65–79, feb 2017. [Online]. Available: <https://linkinghub.elsevier.com/retrieve/pii/S104620231730083X>
- [45] K. Kretzschmar and F. M. Watt, "Lineage tracing," *Cell*, vol. 148, no. 1-2, pp. 33–45, jan 2012. [Online]. Available: <https://linkinghub.elsevier.com/retrieve/pii/S0092867412000037>
- [46] F. Amat, W. Lemon, D. P. Mossing, K. McDole, Y. Wan, K. Branson, E. W. Myers, and P. J. Keller, "Fast, accurate reconstruction of cell lineages from large-scale fluorescence microscopy data," *Nature Methods*, vol. 11, no. 9, pp. 951–958, sep 2014. [Online]. Available: <http://www.nature.com/articles/nmeth.3036>
- [47] D. J. Flannigan and A. H. Zewail, "4D electron microscopy: principles and applications," *Accounts of Chemical Research*, vol. 45, no. 10, pp. 1828–1839, oct 2012. [Online]. Available: <http://pubs.acs.org/doi/10.1021/ar3001684>
- [48] G. Lu and B. Fei, "Medical hyperspectral imaging: a review," *Journal of Biomedical Optics*, vol. 19, no. 1, p. 010901, jan 2014. [Online]. Available: <http://biomedicaloptics.spiedigitallibrary.org/article.aspx?doi=10.1117/1.JBO.19.1.010901>
- [49] W. Jahr, B. Schmid, C. Schmied, F. O. Fahrbach, and J. Huisken, "Hyperspectral light sheet microscopy," *Nature Communications*, vol. 6, no. 1, p. 7990, nov 2015. [Online]. Available: <http://www.nature.com/articles/ncomms8990>
- [50] A. Özbek, X. L. Deán-Ben, and D. Razansky, "Optoacoustic imaging at kilohertz volumetric frame rates," *Optica*, vol. 5, no. 7, p. 857, jul 2018. [Online]. Available: <https://www.osapublishing.org/abstract.cfm?URI=optica-5-7-857>
- [51] M. K. Miller and R. G. Forbes, *Atom-Probe Tomography*. Boston, MA: Springer US, 2014. [Online]. Available: <http://link.springer.com/10.1007/978-1-4899-7430-3>